

# Testing the accuracy of the Hydro-PM approximation in numerical simulations of the Lyman- $\alpha$ forest

Matteo Viel<sup>1</sup>, Martin G. Haehnelt<sup>1</sup> & Volker Springel<sup>2</sup>

<sup>1</sup> *Institute of Astronomy, Madingley Road, Cambridge CB3 0HA*

<sup>2</sup> *Max-Planck-Institut für Astrophysik, Karl-Schwarzschild-Str. 1, Garching bei München, Germany*

15 October 2018

## ABSTRACT

We implement the hydro-PM (HPM) technique (Gnedin & Hui 1998) in the hydrodynamical simulation code GADGET-2 and quantify the differences between this approximate method and full hydrodynamical simulations of the Lyman- $\alpha$  forest in a concordance  $\Lambda$ CDM model. At redshifts  $z = 3$  and  $z = 4$ , the differences between the gas and dark matter (DM) distributions, as measured by the one-point distribution of density fluctuations, the density power spectrum and the flux power spectrum, systematically decrease with increasing resolution of the HPM simulation. However, reducing these differences to less than a few percent requires a significantly larger number of grid-cells than particles, with a correspondingly larger demand for memory. Significant differences in the flux decrement distribution remain even for very high resolution hydro-PM simulations, particularly at low redshift. At  $z = 2$ , the differences between the flux power spectra obtained from HPM simulations and full hydrodynamical simulations are generally large and of the order of 20-30%, and do not decrease with increasing resolution of the HPM simulation. This is due to the presence of large amounts of shock-heated gas, a situation which is not adequately modelled by the HPM approximation. We confirm the results of Gnedin & Hui (1998) that the statistical properties of the flux distribution are discrepant by  $\gtrsim 5 - 20\%$  when compared to full hydrodynamical simulations. The discrepancies in the flux power spectrum are strongly scale- and redshift-dependent and extend to large scales. Considerable caution is needed in attempts to use calibrated HPM simulations for quantitative predictions of the flux power spectrum and other statistical properties of the Lyman- $\alpha$  forest.

**Key words:** Cosmology: intergalactic medium – large-scale structure of universe – quasars: absorption lines – hydrodynamics – methods: numerical

## 1 INTRODUCTION

The prominent absorption features blue-ward of the Lyman- $\alpha$  emission in the spectra of high-redshift quasars (QSOs) are believed to arise from smooth density fluctuations of a photoionised warm intergalactic medium which trace the dark matter distribution in a relatively simple manner (see Rauch 1998 and Weinberg et al. 1999 for reviews). As a result, the flux power spectrum of this ‘Lyman- $\alpha$  forest’ has become a powerful quantitative probe of the matter power spectrum on scales of  $1 h^{-1}$  to  $40 h^{-1}$  Mpc at redshifts  $z = 2 - 4$ . At these scales and redshifts, the matter distribution is linear or mildly non-linear, a regime that can be accurately modelled with numerical simulations. Such simu-

lations have been used to obtain quantitative estimates of the clustering amplitude and constraints on cosmological parameters from the Lyman- $\alpha$  forest (Croft et al. 1998; Croft et al. 1999; McDonald et al. 2000; Hui et al. 2001; Croft et al. 2002; McDonald 2003; Viel et al. 2003; Viel, Haehnelt & Springel 2004; Viel, Weller & Haehnelt 2004; McDonald et al. 2004a; Desjacques & Nusser 2004) or on astro-physical parameters (Theuns et al. 1998, Meiksin et al. 2001, McDonald et al. 2004b, Bolton et al. 2005).

Unfortunately, the flux power spectrum does not only depend on the dark matter (DM) distribution but also on the thermal state of the intergalactic medium (IGM), and possibly on feedback effects due to star formation and active galactic nuclei (AGN). Ideally, one

would like to use simulations which not only take into account the non-linear gravitational clustering of the matter distribution but also all the relevant hydrodynamics of the gas, including effects of galaxy formation physics, such as radiative cooling and heating, star formation and winds driven by stellar associations or AGN. However, full hydrodynamical simulations of the Lyman- $\alpha$  forest are computationally very demanding. This makes their use for extensive parameter studies difficult. In addition, some physical processes, such as the feedback mechanisms, are still poorly understood. Thus, the use of approximate numerical calculations of the flux distribution of the Lyman- $\alpha$  forest very attractive, an approach that has been widely applied in previous work (e.g. McGill 1990; Hui et al. 1997; Meiksin & White 2001; Viel et al. 2002b; Zhan et al. 2005). Note that such approximate calculations of the Lyman- $\alpha$  flux distribution have been crucial in establishing the modern paradigm for the origin of the Lyman- $\alpha$  forest in the first place (Bi 1993, Bi & Davidsen 1997, Viel et al. 2002a).

In 1998, Gnedin & Hui (GH) have proposed the ‘Hydrodynamic Particle-Mesh method’ (HPM) as an efficient numerical method to approximate the formation and evolution of the Lyman- $\alpha$  forest. This technique is based on a particle-mesh (PM) approach for following the evolution of dark matter. The gravitational potential of the PM solver is then modified with an effective potential which mimics the effect of gas pressure. GH found that global statistical properties of the flux distribution in HPM simulations are accurate to  $\sim 5 - 20\%$  when compared to full hydrodynamical simulations. This prompted e.g. McDonald et al. (2004a) to use HPM simulations that were calibrated with a small number of hydrodynamical simulations to obtain predictions of the flux power spectrum for a wide range of cosmological and physical parameters describing the thermal state of the gas.

The statistical errors of the flux power spectrum obtained from high-resolution Echelle spectra are  $\sim 4\%$  and can in principle become as small as a few percent for large samples of low-resolution spectra (e.g. Kim et al. 2004, McDonald et al. 2005). This has opened up the exciting prospect to use the Lyman- $\alpha$  forest to constrain inflationary parameters and the nature of dark matter, based on high accuracy measurements of the DM power spectrum inferred from the Lyman- $\alpha$  forest (Viel, Weller & Haehnelt 2004; Seljak et al. 2004; Viel et al. 2005). However, a prerequisite is the availability of accurate predictions of the flux power spectrum for a wide range of parameters.

The hydrodynamical code GADGET-2 (Springel, Yoshida & White 2001; Springel 2005), which we have used extensively in earlier work for full hydrodynamical simulations of the Lyman- $\alpha$  forest (Viel, Haehnelt & Springel 2004; Bolton et al. 2005), is a TreeSPH code which also offers a PM algorithm which can optionally be used to calculate long-range gravitational forces. In this code the HPM method of GH can therefore be easily implemented. This makes GADGET-2 well suited for a detailed analysis of the accuracy and systematic uncertainties of the HPM method by comparing simulations

run with it to full hydrodynamical TreeSPH-PM simulations.

In this paper, we perform such an analysis and investigate the dependence of the discrepancies between HPM and full hydrodynamical simulations on a range of numerical parameters for the relevant redshift range  $z = 2 - 4$ . Note that we here do not intend to optimize the HPM method.

The outline of the paper is as follows. In Section 2, we briefly describe the hydrodynamical code GADGET-2 and we review the basic equations of the HPM formalism. We also show that the HPM implementation of GADGET-2 and the HPM code by Gnedin & Hui give similar results for a suitable choice of numerical parameters. In Section 3, we discuss the differences between our HPM implementation and full hydrodynamical simulation by analysing the statistical properties of the flux distribution. We further analyse the effect of shock heating, the influence of various numerical parameters on the results, and the CPU time and memory requirements. Finally, Section 4 contains a summary and our conclusions.

## 2 SIMULATION METHODS OF THE Lyman- $\alpha$ FOREST

### 2.1 Full hydrodynamical simulations

The hydrodynamical simulation code GADGET-2 (Springel, Yoshida & White 2001; Springel 2005) can optionally employ a PM technique to calculate long-range gravitational forces, resulting in a ‘TreePM’ scheme for gravitational forces. We will use hydrodynamical simulations run with this SPH/TreePM implementation of GADGET-2 as “reference” simulations to assess in detail the accuracy and systematic uncertainties of the approximate HPM method. The TreePM approach speeds up the calculation of long-range gravitational forces considerably compared to a tree-only implementation.

All our simulations were performed with periodic boundary conditions and an equal number of dark matter and gas particles. We employ the ‘entropy-formulation’ of SPH proposed by Springel & Hernquist (2002). Radiative cooling and heating processes are followed using an implementation similar to that of Katz et al. (1996) for a primordial mix of hydrogen and helium. We have assumed a mean UV background produced by quasars as given by Haardt & Madau (1996), which leads to reionisation of the Universe at  $z \simeq 6$ . The simulations are run with heating rates increased by a factor of 3.3 in order to achieve temperatures which are close to observed temperatures (Abel & Haehnelt 1999, Schaye et al. 2000, Ricotti et al. 2000).

In order to maximise the speed of the dissipative hydrodynamical simulations we have employed a simplified star-formation criterion in the majority of our runs. All gas at densities larger than 1000 times the mean density was turned into collisionless stars. The absorption systems producing the Lyman- $\alpha$  forest have small overdensity so this criterion has little effect on flux statistics, while speeding up the calculation by a factor

of  $\sim 6$ , because the small dynamical times that would otherwise arise in the highly overdense gas need not to be followed. In a pixel-to-pixel comparison with a simulation which adopted the full multi-phase star formation model of Springel & Hernquist (2003) we explicitly checked for any differences introduced by this approximation. We found that the differences in the flux probability distribution function were smaller than 2%, while the differences in the flux-power spectrum were smaller than 0.2 %. We have also turned off all feedback options of GADGET-2 in our simulations. An extensive resolution and box size study has been performed in Viel, Haehnelt & Springel (2004) and in Bolton et al. (2005).

For all simulations presented here we have adopted a box size of 30 comoving  $h^{-1}$  Mpc and the cosmological parameters  $\Omega_{\text{om}} = 0.26$ ,  $\Omega_{\text{0A}} = 0.74$ ,  $\Omega_{\text{0b}} = 0.0463$  and  $H_0 = 72 \text{ km s}^{-1} \text{ Mpc}^{-1}$ ,  $\sigma_8 = 0.85$  and  $n = 0.95$  (the parameters of the B2 simulation in Viel, Haehnelt & Springel 2004). The CDM transfer functions of all models have been taken from Eisenstein & Hu (1999).

## 2.2 HPM implementation of GADGET-2

GH proposed to introduce an effective potential that mimics gas pressure into an otherwise collisionless dark matter simulation, carried out with a particle mesh code. This method has become known as Hydro-Particle-Mesh (HPM) approximation. The idea of the HPM approximation is to take advantage of the fact that the low density IGM responsible for most of the Lyman- $\alpha$  forest absorption obeys a simple relation between gas density and gas temperature, which is well described by a power-law ‘equation of state’:

$$T = T_0(z) (1 + \delta)^{\gamma(z)-1}. \quad (1)$$

The evolution of  $T_0$  and  $\gamma$  with redshift depends on the reionisation history (Hui & Gnedin 1997). The ‘equation of state’ predicts the temperature of gas of given density to better than 10% for the low density IGM where shock heating is not important. Instead, the temperature is set by a balance between photoionisation heating and adiabatic cooling due to the expansion of the universe.

Based on the density alone, equation (1) also allows an estimate of the thermal pressure which enters the equation of motion for a cosmic gas element. We know from full hydrodynamical simulations that the baryons follow the dark matter generally well apart from high density regions where pressure effects on small scales become important. GH suggested therefore to use the density of the dark matter in a PM simulation together with Eqn. (1) to estimate the temperature and pressure of the gas. One can then obtain the acceleration on a cosmic gas element due to the gradient of the pressure as

$$\frac{d\mathbf{v}}{dt} + H\mathbf{v} = -\nabla\phi - \frac{1}{\rho}\nabla P, \quad (2)$$

where  $\mathbf{v}$  is the gas peculiar velocity,  $\phi$  is the gravitational potential, and  $P$  is the thermal pressure. If the gas is highly ionised (so that the mean molecular weight is roughly constant, which is true for the Lyman-alpha forest), and the temperature is a function of density

only, so that  $P = P(\rho)$ , equation (2) can be reduced to the expression

$$\frac{d\mathbf{v}}{dt} + H\mathbf{v} = -\nabla\psi, \quad (3)$$

where

$$\psi = \phi + \mathcal{H}, \quad (4)$$

and  $\mathcal{H}$ , the *specific enthalpy*, is

$$\mathcal{H}(\rho) = \frac{P(\rho)}{\rho} + \int_1^\rho \frac{P(\rho')}{\rho'^2} d\rho'. \quad (5)$$

Equation (3) is identical to the equation of motion for the collisionless dark matter except that the usual gravitational potential  $\phi$  is replaced by an effective potential  $\psi$ , which takes into account both gravity and thermal pressure. Since the gravitational potential  $\phi$  has to be computed from the density field in a regular PM simulation anyway, computing the enthalpy adds only a modest computational overhead.

We have implemented this HPM method in the simulation code GADGET-2. We closely follow the approach of GH with only a few minor differences. In the HPM code of GH, only one set of particles was used, i.e. the fact that the dark matter does not feel the pressure on small scales was neglected. As GADGET-2 is a SPH code which treats DM and baryons separately, we kept this distinction in our HPM implementation. This may result in some small differences on small scales. In Section 2.3, we will compare simulations with the HPM implementation of GADGET-2 to runs carried out with the HPM code of GH (kindly provided by Nick Gnedin).

There are three numerical parameters defining the technical details of our HPM implementation in GADGET-2. The first parameter is the number of cells of the PM grid. We describe this by  $N_{\text{grid}}$ , the number of cells per dimension. The second parameter,  $H_s$ , describes the scale of the smoothing applied to the enthalpy field before taking its spatial derivative. The density and enthalpy fields are more sensitive to shot noise than the gravitational potential, because for the latter, high frequency noise is suppressed as  $\phi(k) \propto \delta_k k^{-2}$ . We have thus followed GH and apply a Gaussian smoothing to the density field before computing the enthalpy and its spatial derivative. We apply a smoothing factor  $\exp(-k^2 h_s^2)$  to the density field in Fourier space, where  $h_s = H_s L / N_{\text{grid}}$ . The third numerical parameter,  $r_s = A_s L / N_{\text{grid}}$ , is the scale of the smoothing of the PM force, which we usually express in terms of  $A_s$ , i.e. in units of the mesh cell size. The parameter  $A_s$  hence controls the level of residual force anisotropies in the PM force. In the TreePM code,  $r_s$  also gives the scale of the short-range/long-range force split. We will discuss the choice of numerical values for these parameters in Section 3.3. Note that the HPM code of GH has only two parameters  $N_{\text{grid}}$  and  $H_s$ , i.e. no attempt is made to make the PM force more isotropic on the scale of the mesh. GH have adopted the choice  $H_s = 3$ .

To fix the slope and normalisation of the power-law temperature-density relation of the IGM, our code follows the thermal history of two fiducial gas elements at density values equal to the mean cosmic density and

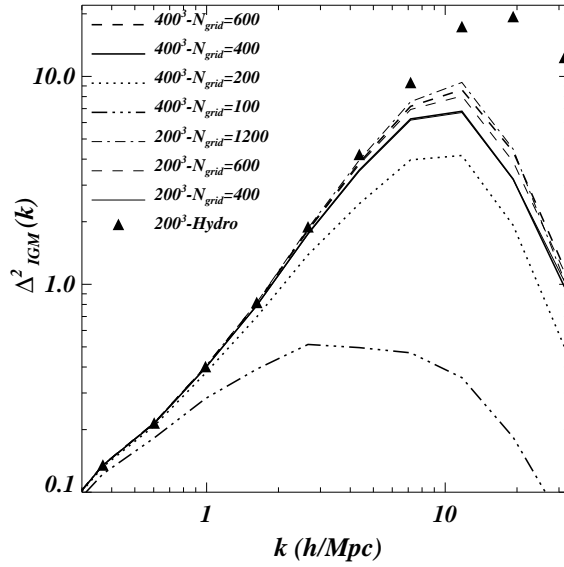


**Figure 1.** Power spectrum of the gas density field of the HPM simulations run with GADGET-2 at  $z = 3$ , at two different resolutions and for several different values of the parameter  $N_{\text{grid}}$ . The power spectrum of the full hydrodynamical simulation is represented by the filled triangles.

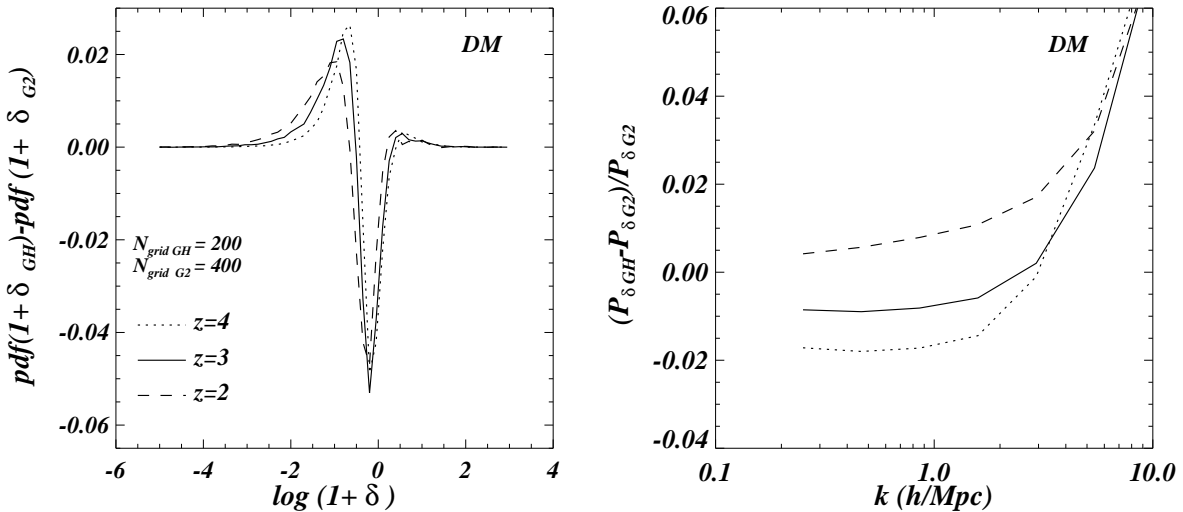


**Figure 2.** *Left:* differences in the probability distribution functions of the dark matter density field between GADGET-2 (G2) and the Gnedin & Hui (GH) code. Both of them have been run in the PM mode with a grid of  $200^3$  for GH and  $400^3$  for G2. *Right:* Fractional differences in the 3D matter power spectrum. The results are shown at three different redshifts  $z = 2, 3, 4$  as dashed, continuous and dotted curves, respectively.

at 1.1 times the mean cosmic density. For a specified evolution of the ionising UV background, we can then compute the values of  $T_0$  and  $\gamma$  from the temperatures attained by these two fiducial gas elements.

In Figure 1, we compare the 3D gas power spectrum for a range of HPM simulations with different particle numbers and mesh sizes with a full hydrodynamical simulation with  $200^3$  dark matter and  $200^3$  gas parti-

cles (shown as triangles). All simulations were run with GADGET-2. We only show results at  $z = 3$ , but note that the results at  $z = 2$  and  $z = 4$  are very similar. On large scales ( $k < 6 h/\text{Mpc}$ ), the power spectrum of the gas distribution of HPM simulations converges nicely to that of the full hydrodynamical simulation when the resolution of the mesh used for calculating the gravitational forces is increased. Note, however, that even

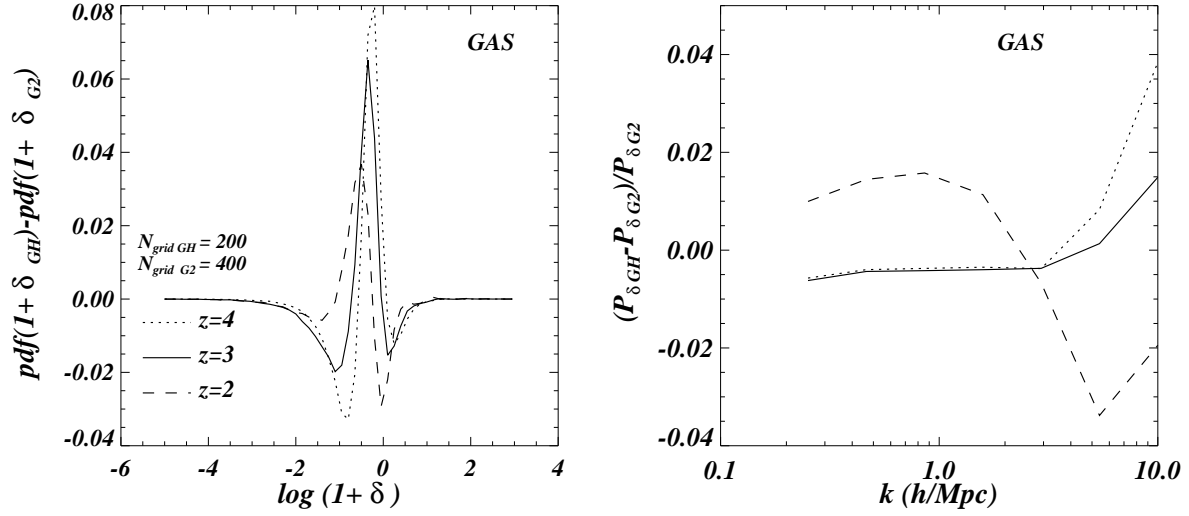


**Figure 3.** *Left:* differences in the probability distribution functions of the gas density field between simulations run with GADGET-2 (G2) and the Gnedin & Hui (GH) code. Both of them have been run in the HPM mode with a grid of  $200^3$  for GH and  $400^3$  for G2. *Right:* Fractional differences in the 3D matter power spectrum. The results are shown at three different redshifts  $z = 2, 3, 4$  as dashed, continuous and dotted curves, respectively.

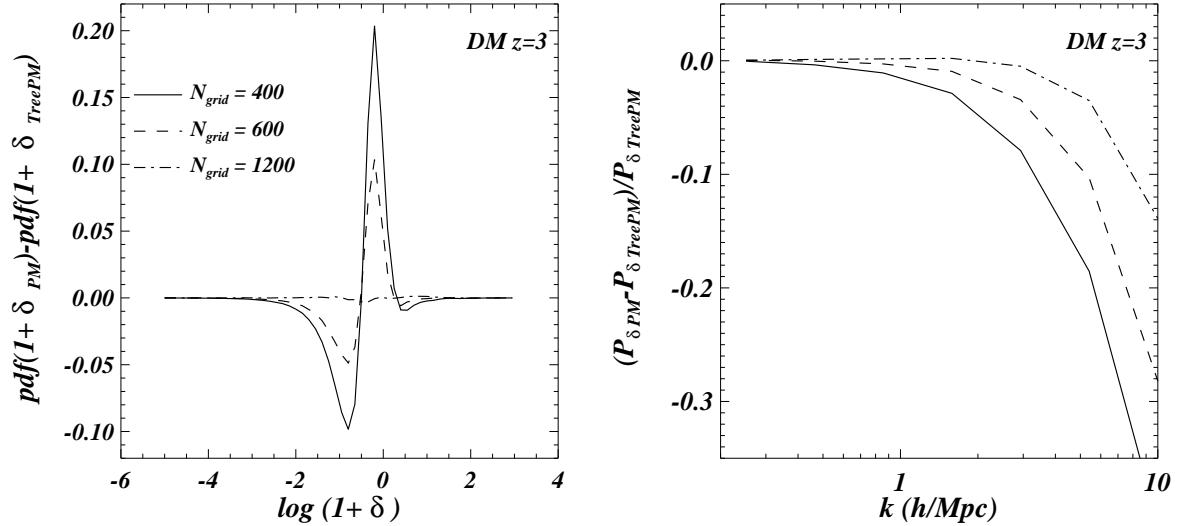


**Figure 4.** *Left:* differences in the probability distribution functions of the dark matter density field between simulations run with GADGET-2 in its HPM and in its TreePM mode (the PM grid for the TreePM run is fixed to the value  $N_{\text{grid}} = 200$ ). *Right:* Fractional differences in the 3D matter power spectrum. The results are shown at  $z = 3$  and for three different values of  $N_{\text{grid}}$  (400, 600, 1200) as continuous, dashed and dot-dashed curves, respectively.

for very high resolution (six times more mesh cells in the HPM simulation than particles in the full hydrodynamical simulation) the power on small scales in the HPM simulations is significantly smaller than that in the full hydrodynamical simulations. Note further that changing the mesh resolution is more important than changing the particle number in the HPM simulations. The thin and thick solid curves are for HPM simulations with the same grid resolution but a factor eight

different particle number. They are virtually identical. We also note that the results and trends for the dark matter power spectrum are qualitatively similar. In the runs discussed in the following, we will use the HPM implementation of GADGET-2 with  $2 \times 200^3$  particles and with  $N_{\text{grid}} \geq 200$ .

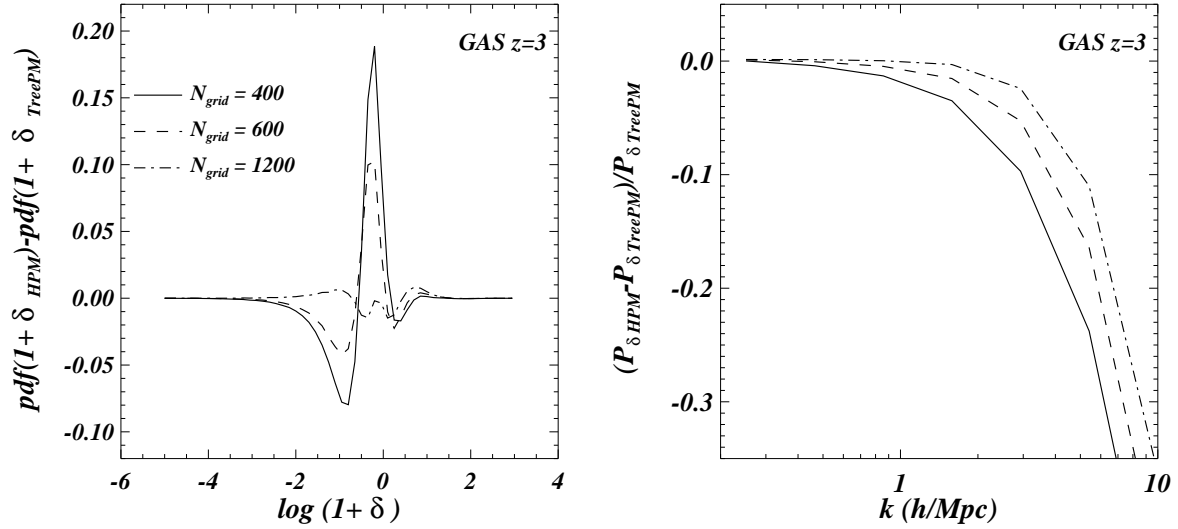


**Figure 5.** *Left:* differences in the probability distribution functions of the gas density field between simulations run with GADGET-2 in its HPM and in its TreePM mode (the PM grid for the TreePM run is fixed to the value 200). *Right:* Fractional differences in the 3D matter power spectrum. The results are shown at  $z = 3$  and for three different values of  $N_{\text{grid}}$  (400, 600, 1200) as continuous, dashed and dot-dashed curves, respectively.

### 2.3 Comparison between the HPM implementation of GADGET-2 and the HPM code of Gnedin & Hui

In this section we compare the gas and dark matter distribution of simulations run with the HPM implementation of the GADGET-2 code and the HPM code of GH. We use the same initial conditions and temperature-density relation. At  $z = 2, 3$ , and  $4$ ,  $T_0$  and  $\gamma$  ( $T_0, \gamma$ ) have the following values: (21500 K, 1.505), (21500 K, 1.524) and (19200 K, 1.536).

In Figures 2 and 3, we show the relative differences of the probability distribution and the power spectrum of the *dark matter* and *gas* density at redshifts  $z = 2$ ,  $z = 3$ , and  $z = 4$ . We have varied the resolution of the mesh to calculate the gravitational force in the HPM implementation of GADGET-2 in steps of factors of two. The other two relevant parameters in the GADGET-2 runs have been set to  $H_s = 3$  and  $A_s = 1.25$ . For the case shown in Figures 2 and 3, the grid resolution for the HPM implementation of GADGET-2 was a factor two higher than that used for the HPM code of GH. In this case the agreement was best, better than 5% (dark matter) and 8% (gas) for the probability distribution function\* (pdf) and better than 2% for power spectra at wavenumbers relevant for constraining cosmological parameters with the Lyman- $\alpha$  forest,  $0.3 \lesssim k \text{ (h/Mpc)} \lesssim 3$  (Viel, Haehnelt & Springel 2004). Because of the smoothing applied to the PM force in GADGET-2, a somewhat finer mesh is needed to match the results of the HPM code by GH, where

(CODE, # part.)	$N_{\text{grid}}$	CPU-time (ks)	Mem. (Gb)
HPM-200 <sup>3</sup>	100	1.5	3
HPM-200 <sup>3</sup>	200	3.1	3.5
HPM-200 <sup>3</sup>	400	4.7	4.5
HPM-200 <sup>3</sup>	600	11.2	12
HPM-200 <sup>3</sup>	1200	15	76
HPM-400 <sup>3</sup>	100	33	26
HPM-400 <sup>3</sup>	200	35	28
HPM-400 <sup>3</sup>	400	40	30
HPM-400 <sup>3</sup>	600	44	36
Hydro-200 <sup>3</sup>	200	183	3.2
Hydro-400 <sup>3</sup>	400	11700	26
GH HPM-200 <sup>3</sup>	200	5.4	3.5

**Table 1.** CPU-time required to reach  $z = 2$  for simulations of a 30 Mpc/h box  $\Lambda$ CDM model and for several different resolutions and values of the parameter  $N_{\text{grid}}$ . The memory required is shown in the last column. All the values are wall-clock times for 32 CPUs (1.3 GHz Itanium 2) of the SGI Altix 3700 (COSMOS) at DAMTP (Cambridge).

such a smoothing is not carried out and larger force anisotropies on the mesh scale are accepted. By reducing  $A_s$ , the agreement of the two codes could be improved further. The two HPM codes agree very well. In the following we will only use the HPM implementation of GADGET-2 but our results should apply similarly to the GH code.

\* The pdf is defined as the number of points or pixels in a given x-axis bin with the property that its integral along the x-coordinate is one.

### 3 COMPARISON BETWEEN FULL HYDRODYNAMICAL AND HPM SIMULATIONS

#### 3.1 The dark matter and gas density fields

We first want to check the agreement of the dark matter and gas distributions between simulations run with the TreePM and HPM implementations of GADGET-2. In Figure 4, we show the differences in the density pdf and the power spectrum for the dark matter distribution at  $z = 3$ , for three different values of  $N_{\text{grid}}$  used in the HPM simulation. The results at  $z = 2$  and  $z = 4$  are similar. The simulations were run with  $200^3$  and  $2 \times 200^3$  particles, respectively. In the simulation with the Tree-PM implementation, the number of mesh cells of the PM grid was set equal to the number of particles. As also expected from the results shown in Fig. 1, the differences become smaller with increasing resolution of the PM grid used for the HPM implementation. The differences in the pdf of the DM density are smaller than 10% (20%) for  $N_{\text{grid}}=600$  (400). If a very fine mesh of dimension  $N_{\text{grid}}=1200$  is used, the pdf of the HPM simulation is indistinguishable from that of the full hydrodynamical TreePM simulation. For  $N_{\text{grid}}=600$  (400) the discrepancy in the dark matter power spectrum (right panel) is less than 2% (4%) for  $0.2 < k(h/\text{Mpc}) < 2$ . For  $N_{\text{grid}}=1200$ , the difference is less than 0.5% in the same range of wavenumbers. At larger wavenumber the differences in the power spectra become much larger due to the much higher resolution achieved with the TreePM code. Note, however, that these small scales are not used for the recovery of the dark matter power spectrum from the Lyman- $\alpha$  forest because of the uncertainties in the flux power spectrum due to the thermal history and the metal contamination of the IGM (Kim et al. 2004).

Figure 5 shows the difference in the gas distributions between simulations with the HPM and TreePM implementations. The differences are similar to those found in the dark matter distribution.

#### 3.2 Flux statistics

##### 3.2.1 The flux probability distribution function

The flux distribution in the Lyman- $\alpha$  forest depends on the spatial distribution, the peculiar velocity field and the thermal properties of the gas. In the last section, we have shown that the gas distribution of the HPM simulations converges rather well to that of the full hydrodynamical simulations when the resolution of the PM mesh is improved. For the flux distribution the situation is more complicated, however. In Figure 6, we plot the differences in the pdf of the flux for HPM simulations with a range of  $N_{\text{grid}}$  values compared with the full hydrodynamical simulations at  $z = 2, 3, 4$ . The simulations are the same as those discussed in section 3 and shown in figures 4 and 5 (these figures show results only at  $z = 3$ ). The curves without symbols show the results for the same amplitude of the ionising UV background as in the full hydrodynamical simulations. Note that this means that the flux distribution has *not* been rescaled to a fixed mean flux, as it is often done. Such

a rescaling would mask the numerical effects we seek to identify here. However, to facilitate comparison with other work (e.g. McDonald et al. 2004a), the curves with triangles show the pdf of the flux after re-scaling the flux distribution of the  $N_{\text{grid}} = 1200$  HPM simulation such that the mean transmitted flux is the same as in the full hydrodynamical simulations.

At  $z = 3$ , the flux distribution of the HPM simulations converges reasonably well to that of the full hydrodynamical simulations. With the exception of flux levels  $F > 0.8$ , the differences are smaller than 5% for  $N_{\text{grid}} = 600$  and even smaller for higher resolutions of the PM mesh. In regions of low absorption ( $F > 0.8$ ) the differences are, however, large (10-20%), change sign with increasing resolution, and do not converge. We have inspected a few spectra individually and found that the discrepancy is due to differences in both density and temperature in the lowest density regions. At  $z = 4$  these differences in regions of low absorption are substantially larger. Because of the strong decrease of the mean flux with increasing redshift, these regions correspond to significantly more underdense regions than at  $z = 3$ . At  $z = 2$  additional large differences up to 50% arise in regions of strong absorption, which also do not vanish with increasing resolution. For the  $N_{\text{grid}} = 1200$  HPM simulation, the overall agreement with the full hydrodynamical simulation is of the order of 2% for  $F < 0.85$  at  $z = 3, 4$ , while at  $z = 2$ , discrepancies of the order of  $\gtrsim 10\%$  remain both in underdense and very dense regions. The differences at  $z = 2$  and for  $F < 0.15$  are due to the gas in dense regions being substantially colder in the HPM simulations than in the full hydrodynamical simulation where a significant portion of the dense gas is shock heated. In Figure 6 we overplot the results from a higher resolution HPM run with  $2 \times 400^3$  particles and  $N_{\text{grid}} = 600$  as a long dashed line with filled diamonds. The results are very similar to the HPM simulation with  $2 \times 200^3$  particles and  $N_{\text{grid}} = 200$ . We hence confirm the findings of GH that the differences in the flux pdf between HPM and full hydrodynamical simulations are of the order of 10-15%.

##### 3.2.2 The flux power spectrum

The main motivation of the use of HPM simulations comes presently from the need for accurate predictions of the flux power spectrum for a wide range of astrophysical and cosmological parameters. Such a grid of predictions allows a detailed comparison with observational data and a determination of best-fit values and confidence intervals of cosmological parameters (McDonald et al. 2004a).

In Figure 7, we plot the differences of the flux power spectrum of HPM simulations with a range of mesh sizes compared with full hydrodynamical simulations at  $z = 2, 3, 4$ . The simulations are the same as those discussed in the previous sections. As in figure 6, the curves without symbols show results for the same amplitude of the ionising UV background while the curves with empty triangles show the flux power spectrum after rescaling the flux distribution of the  $N_{\text{grid}} = 1200$  HPM simulation such that the mean flux is the same

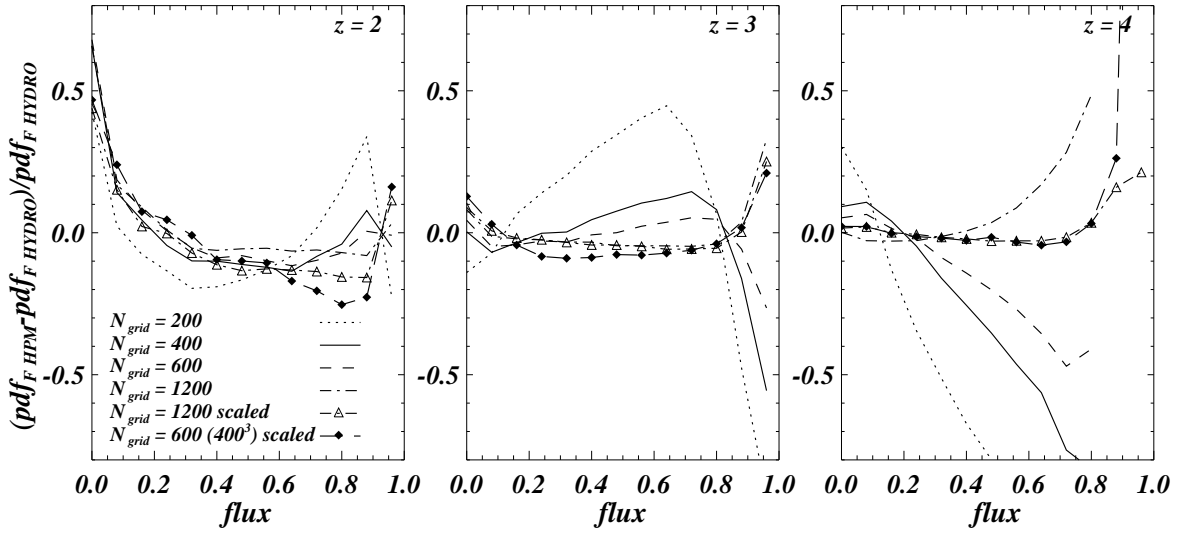


**Figure 6.** Effect of the parameter  $N_{\text{grid}}$  for simulations of a 30 Mpc/h box with  $2 \times 200^3$  (gas and dm) particles. *Left panel:* Fractional differences between the probability distribution functions of simulations with  $N_{\text{grid}}=200$  (dotted),  $N_{\text{grid}}=400$  (continuous),  $N_{\text{grid}}=600$  (dashed), and  $N_{\text{grid}}=1200$  (dot-dashed) at  $z = 2$ . Also shown is the full hydrodynamical TreePM simulation with  $N_{\text{grid}}=200$  and with the same initial conditions. The long-dashed line with filled diamonds represents results for the higher resolution run with  $2 \times 400^3$  particles and with  $N_{\text{grid}}=600$ . The other HPM parameters have been fixed to the fiducial values described in the text. The dot-dashed curve with overplotted empty triangles is for a simulation with  $N_{\text{grid}}=1200$  for which the simulated flux has been scaled to match the value of the full hydro simulations, in the other cases the spectra have not been scaled (see text for the details). *Middle Panel:* Results at  $z = 3$ . *Right Panel:* Results at  $z = 4$ .

as in the full hydrodynamical simulations. In Figure 7 we show the results from a higher resolution HPM run with  $2 \times 400^3$  particles and  $N_{\text{grid}} = 600$ , as the long-dashed line with overplotted filled diamonds. At redshift  $z = 4$  and  $z = 3$  there is perfect agreement with the  $N_{\text{grid}} = 1200$  HPM simulation, in the wavenumber range of interest here. At  $z = 2$  there are small differences of the order of  $< 5\%$ . Thereby, increasing the number of particles does not improve the agreement significantly.

At redshifts  $z = 3$  and  $z = 4$ , the flux power spectra of the HPM simulations converge well to those of the full hydrodynamical simulations, but only for resolutions of the PM mesh where the number of the mesh cells is substantially larger than that of the number of particles in the full hydrodynamical simulations. At  $z = 3$ , the HPM simulations with  $N_{\text{grid}}=400$  (600) have *scale-dependent* differences of about 10% (7%) in the wavenumber range relevant for inferring the matter power spectrum. For  $N_{\text{grid}}=1200$ , there is a scale-independent offset of about 5% (3% when rescaled to the same mean flux). At redshift  $z = 4$  the situation is very similar. However, at redshift  $z = 2$ , the flux power spectrum of the HPM simulations does not converge to that of the full hydrodynamical simulation. The differences are here actually smallest for the HPM simulation with lowest resolution ( $N_{\text{grid}}=200$ ). However, even in this case the discrepancies are large and strongly scale dependent, of the order of 25-30% at the largest scales. At small scales  $k > 0.02$  s/km, the size of the disagreement and its scale dependence is similar to that found by McDonald et al. (2004a, their figure 5). Note that because of the smaller

box size of their hydro simulations, McDonald et al. were not able to probe scales  $k < 0.007$  s/km (at  $z = 2$ ), where the differences increase dramatically. Note that the amount of shock-heated gas is significantly larger in simulations with larger box-size. To test further to what extent these discrepancies at large scales depend on the resolution of the hydro-simulation, we have run an additional hydro-simulation with 64 times higher mass resolution ( $2 \times 200^3$  particles in a  $7.5 h / \text{Mpc}$  box). There is good agreement with the results shown in Figure 7. We stress here that our goal is to get a good convergence of the flux power in the range  $0.003 < k \text{ (s/km)} < 0.03$ , which is the range which is used for the matter power spectrum reconstruction as in Viel et al. (2004).

These large differences and the lack of convergence appear perhaps counterintuitive considering the rather good convergence of the gas and dark matter distribution. However, they simply originate in the large differences in the pdf of the flux distribution, which in turn are due to the different thermal state of the gas in high density regions in the HPM and full hydrodynamical simulations.

At redshift  $z = 2$ , a larger proportion of the absorption is from gas in high density regions, which is shock-heated in the full hydrodynamical simulations and therefore on average hotter than in the HPM simulations. This tends to mainly affect the strong absorption systems which contribute significantly to the flux power spectrum at large scales (Viel et al. 2004a; McDonald et al. 2004b). We will discuss this further in the next section.

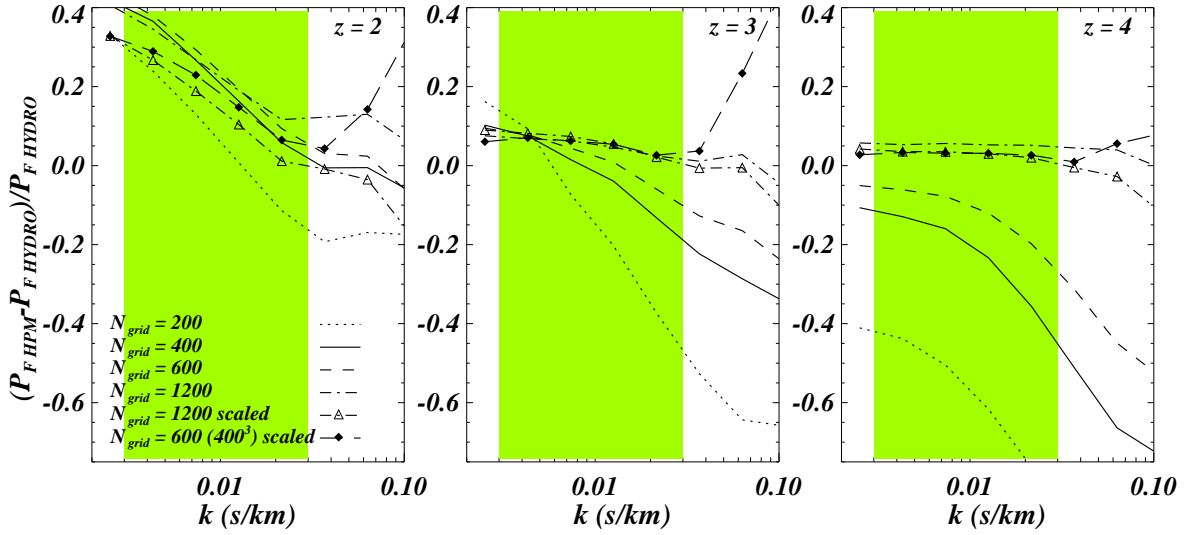


**Figure 7.** Effect of the parameter  $N_{\text{grid}}$  for simulations of a 30 Mpc/h box with  $2 \times 200^3$  (gas and dm) particles. *Left panel:* Fractional differences between the 1D flux power spectra of simulations with  $N_{\text{grid}}=200$  (dotted),  $N_{\text{grid}}=400$  (continuous),  $N_{\text{grid}}=600$  (dashed), and  $N_{\text{grid}}=1200$  (dot-dashed) at  $z=2$ . Also shown is the full hydrodynamical TreePM simulation with  $N_{\text{grid}}=200$  and the same initial conditions. The other HPM parameters have been fixed to the fiducial values described in the text. The dot-dashed curve with overplotted empty triangles is for a simulation with  $N_{\text{grid}}=1200$  for which the simulated flux has been scaled to match the value of the full hydro simulations, in the other cases the spectra have not been scaled (see text for the details). The long-dashed line with filled diamonds represents results for the higher resolution run with  $2 \times 400^3$  particles and with  $N_{\text{grid}}=600$  (results scaled to reproduce the same  $\tau_{\text{eff}}$ ). *Middle Panel:* Results at  $z=3$ . *Right Panel:* Results at  $z=4$ . In all the panels the dashed area represents the range of wavenumbers used by Viel, Haehnelt & Springel (2004) to recover cosmological parameters.

### 3.2.3 Temperature effects on the flux pdf and the flux power spectrum

We have argued that the approximation of the relation between gas density and gas temperature as a power-law breaks down at low redshift. This approximation inevitably does not take into account the amount of moderately shock-heated gas that is falling into the potential wells of the dark matter haloes. In this section, we want to check this explicitly. For this purpose we use the hydrodynamical simulation and the HPM run with  $N_{\text{grid}}=600$ .

As a first step we perform the following simple test. We superimpose onto the full hydro-dynamical SPH simulation the temperature-density relation of the HPM runs, and then recompute the QSO spectra. We find that this results in differences much smaller than those in Figure 7, of order 8%, 5% and 4%, at  $z=2, 3$  and 4, respectively, at the largest scales. Most of the discrepancy is thus indeed due to the differences in the thermal state especially at low redshift. Differences in the thermal state will lead, however, also to pressure differences during the dynamical evolution, which will modify the mass distribution and the peculiar velocity field. In shock fronts, the change in particle trajectories can be substantial. Since the HPM implementation does not capture shocks, it would not treat the dynamics correctly even if the temperatures would be accurate at all times. To investigate this further we have run an SPH simulation with artificial viscosity set to zero and

the temperature-density relation of the HPM simulation. This should mimick an ‘ideal’ HPM simulation: the gravitational force is resolved with high accuracy and in an isotropic way, while the pressure gradients are smooth and resolved everywhere with the maximum resolution allowed by the local particle sampling. The standard HPM method has a less well resolved gravitational force and should be sensitive to over- or under-smoothing of the pressure field in regions of high or low particle density, respectively. The results are shown in Figure 8. The SPH simulation is represented by the dashed line while the dotted line is for the HPM simulation with  $N_{\text{grid}}=1200$  (both the runs have the same number of particles equal to  $2 \times 200^3$ ). There is good agreement with the HPM simulations, suggesting that the discrepancy in the flux power is primarily due to the different thermal state of the gas due to shocks and not to any artefacts of our particular HPM implementation. The total effect on the flux power spectrum should thereby be a combination of an increase of the overall amount of shock-heated gas with decreasing redshift and the change of the mean effective optical depth. The flux power spectrum becomes increasingly sensitive to higher-density gas with decreasing redshift due to the decreasing effective optical depth.

We will now investigate the relation between the differences between HPM and SPH and gradients in the velocity field of the gas. Negative gradients in the peculiar velocity field along the line-of-sight should represent a signature of infalling material and may thus serve as

a rough guide to where shocks occur. In the left panel of Figure 9, we show the ratio of the gas temperatures for the full hydrodynamical simulation and the HPM simulation as a function of the velocity gradient of the gas. We first average the temperature in pixels within 100 km/s from a minimum in the gradient of the peculiar velocity field in real space. Then, we average over the corresponding flux values, in redshift space. Before selecting the negative gradients in the hydrodynamical simulations, we have explicitly checked that the peculiar velocity fields are very similar in both simulations.

The contour plots indicate the number density of points, which varies by a factor of 10 between adjacent contour levels. The bulk of the pixels in this panel is in regions with  $\delta v/\delta x \sim -0.5$  and at ‘hydrodynamical’ temperatures that are about 10% lower than the corresponding temperatures of the HPM simulation. The simulation at  $z = 2$  shows a significantly increased amount of pixels at  $\delta v/\delta x \sim -1$  with HPM temperatures that are colder than the corresponding temperatures in the hydrodynamical simulation. These differences in the temperatures have an important effect on the simulated flux.

In the right panel of Figure 9, we plot the differences in the flux for the same regions of infalling gas. Since the flux is observed in redshift space we have averaged the flux within 100 km/s velocity bins. There are no obvious trends for smaller values of  $\delta v/\delta x$  (i.e. “stronger” shocks). This is due to the fact that stronger shocks have a more complex temperature and density structure which in the hydro simulation is represented more faithfully than in the HPM simulation. As a result, the differences in the temperatures and fluxes actually tend to be averaged out for strong shocks. The scatter for positive values of the gradient  $\delta v/\delta x$  also shows smaller scatter, both in the temperatures ratio and in the flux differences. Most of the differences at  $z = 2$  arise from regions of infalling gas that are not modelled accurately by the HPM method. This suggests that at least part of the discrepancy at low redshift is due to the increased amount of shock-heated gas probed by the Ly- $\alpha$  forest at lower redshift.

### 3.3 The effect of the numerical parameters $H_s$ and $A_s$

As discussed in section 2.2, we need to specify the parameters  $H_s$  and  $A_s$  which describe the smoothing of the gas density and of the gravitational force field in the HPM simulations. There is no obvious optimum choice for these parameters, so a choice needs to be made by comparing to the full hydrodynamical simulations. For changes of  $H_s$ , which controls the smoothing of the pressure field, the resulting differences are very small at large scales (less than 1%). They are only weakly scale- and redshift-dependent and only slightly increase at small scales for  $H_s$  in the range 1.5-3. We have therefore fixed  $H_s = 3$  for all simulations.

Varying the parameter  $A_s$ , which controls the smoothing of the gravitational force field, has a somewhat larger effect. In Figure 10, we show the differences between the flux power spectrum of a HPM ( $N_{\text{grid}} =$

600) simulation and that of the full hydrodynamical simulation for different values of  $A_s$ , at three different redshifts  $z = 2, 3, 4$ . The differences are typically a few percent but can be as large as 10%. It is not obvious which value for  $A_s$  represents an optimum choice. One possibility is to impose a certain requirement for the maximum allowed force anisotropy generated by a point mass in the PM scheme. Using such a criterion, we have set  $A_s = 1.25$ , which gives typical PM force errors less than 1 per cent.

### 3.4 CPU time and memory requirements

In Table 1, we summarise the total CPU time (in wall-clock seconds) required by the simulations to run to  $z = 2$ , and their memory requirement (in Gbytes). We include simulations with a range of particle numbers and resolutions of the PM mesh, all for a box size of 30 Mpc/h. The HPM simulation with  $N_{\text{grid}}=600$  has run about 20 times faster than the hydrodynamical SPH/TreePM simulation at the corresponding resolution, but has a three times larger memory requirement. The  $N_{\text{grid}}=1200$  HPM simulation, which as we saw gave a good agreement with the full hydrodynamical simulations in terms of the gas and dark matter distribution, is still faster than the SPH simulation by a factor 10, but its memory requirement is very large. We note that the simulations with a very high resolution of the PM mesh ( $N_{\text{grid}} = 1200$ ) have been difficult to run because of their very large memory requirement, which is close to the total amount available on the COSMOS computer we used.

## 4 DISCUSSION AND CONCLUSIONS

We have compared full hydrodynamical simulations carried out with the SPH/TreePM code GADGET-2 to simulations that used the HPM method. The latter scheme was implemented by us in GADGET-2, and we compared this implementation with the independent code of GH. Our comparison was performed at redshifts  $z = 2, z = 3$  and  $z = 4$ . Our main results can be summarised as follows.

- The dark matter and gas distributions of HPM simulations with GADGET-2 converge well to the full hydrodynamical simulations with the SPH/TreePM code. For a PM mesh with  $> 6^3$  more mesh cells than particles in the SPH simulations, the difference in the pdf of the gas and matter distributions are less than 1 per cent. The same is true for the matter power spectrum at wavenumbers up to 20 times the fundamental mode of the box for a mesh with  $1200^3$ . At smaller scales the differences in the power spectra strongly increase due to lack of resolution of the HPM grid.

- The pdf of the flux distribution of HPM simulations with GADGET-2 does not converge to that of the full hydro simulations. At low levels of absorption ( $F > 0.8$ ) the differences (10% and more) do not decrease with increasing resolution at all three redshifts examined. At  $z = 2$ , there is an additional large difference at low

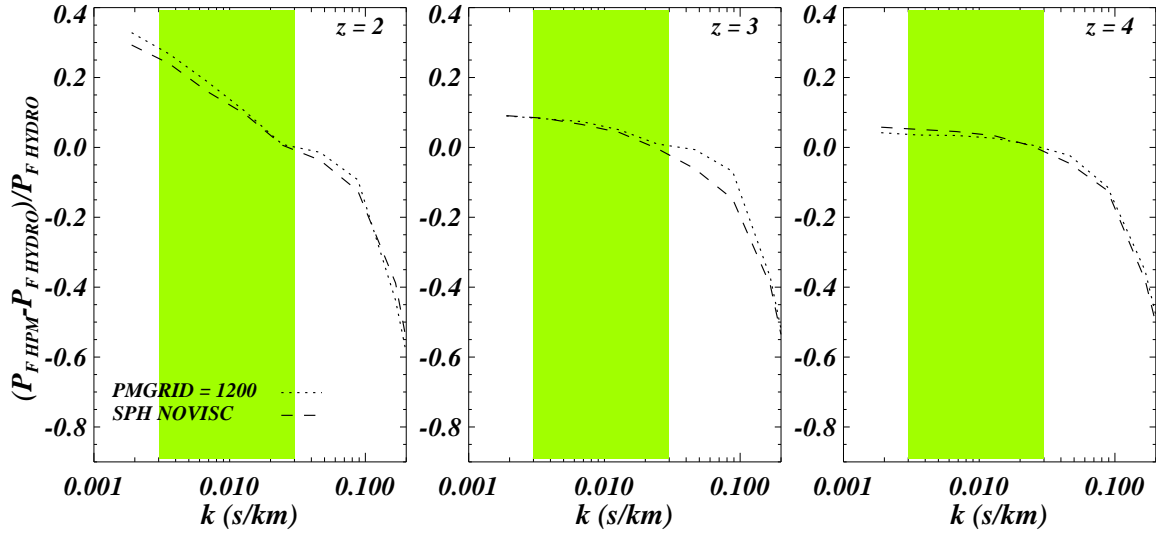


**Figure 8.** Fractional differences between: 1) an HPM simulation with  $2 \times 200^3$  and with  $N_{\text{grid}} = 1200$  and a full SPH hydrodynamical simulation (dotted line); 2) between a SPH simulation with zero artificial viscosity and with a superimposed temperature-density relation of the HPM runs and a full SPH hydrodynamical simulation (dashed line). Results are shown at  $z = 2, 3, 4$  in the left, middle and right panels, respectively. Spectra have been scaled to reproduce the same effective optical depth.

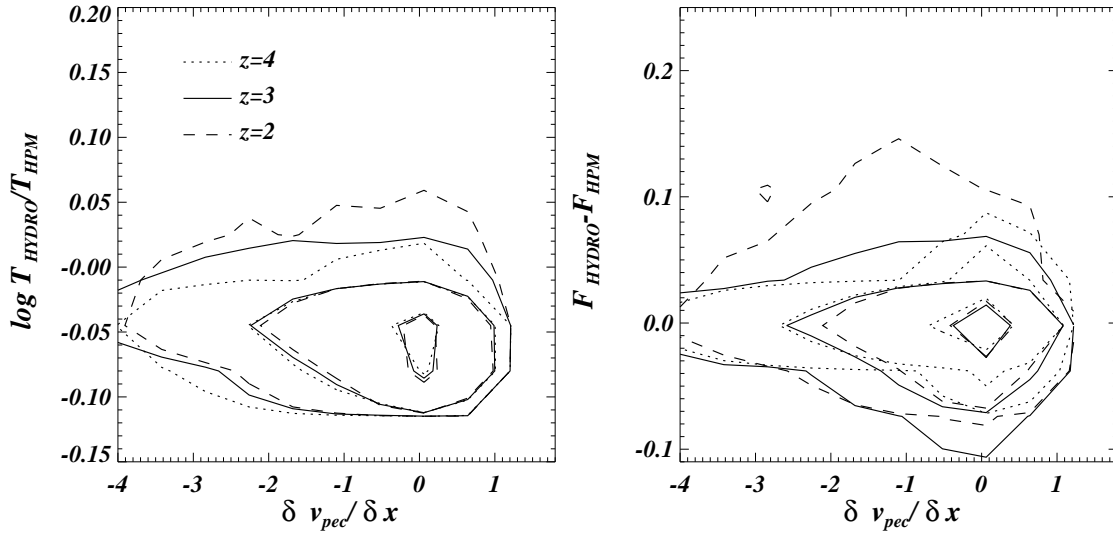


**Figure 9.** Role of shock-heated gas. *Left:* Ratio of the temperatures in simulations run with the full hydro and HPM implementation with  $N_{\text{grid}}=600$  with the same initial conditions, plotted as a function of the gradient of the peculiar velocity field along the line of sight. *Right:* Differences in the simulated flux values. The contour plots represent the number density of points in the 2D plane and the number density increases by an order of magnitude at each contour level. The dashed, continuous and dotted lines are for  $z = 2, 3, 4$ , respectively.

flux levels which rises to 50% at the lowest flux levels. The latter difference is most likely due to the larger proportion of absorption by dense shock-heated gas at  $z = 2$  which is not modelled well by the HPM method.

- At redshifts  $z = 3$  and  $z = 4$ , the flux power spectrum of HPM simulations with GADGET-2 does converge to that of the full hydrodynamical simulations up to a scale independent offset. For a HPM simula-

tion with box size of  $30h^{-1}$  Mpc and a PM mesh with  $1200^3$  cells this offset is about 5%–7% at wave numbers  $0.002 \text{ s/km} < k < 0.05 \text{ s/km}$ . At  $z = 2$ , however, there are large scale-dependent differences between the flux power spectrum of the HPM simulation and the full hydrodynamical simulation which are as large as 20-40%. These differences are again most likely due to the larger

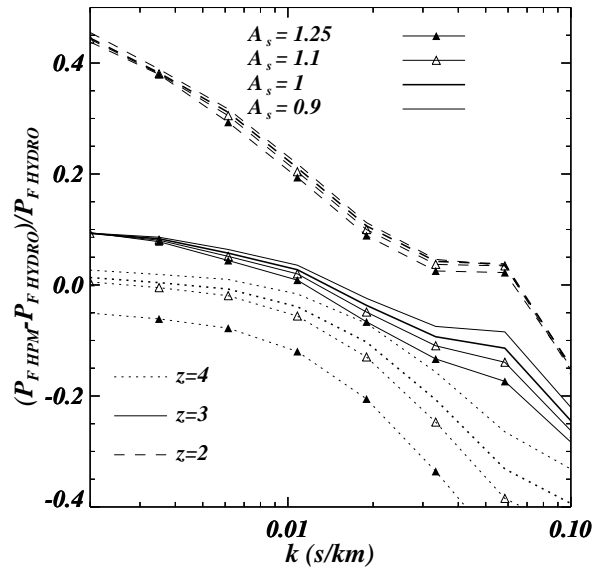


**Figure 10.** Effect of the smoothing parameter  $A_s$  of the HPM implementation in GADGET-2 for simulations of a 30 Mpc/h box with  $2 \times 200^3$  particles. We plot the fractional differences between the 1D flux power spectra of a model with  $A_s$  set to 1.25 (thin line with filled triangles), 1.1 (thin line with empty triangles), 1 (thick line), 0.9 (thin line) and the full hydrodynamical simulation. The results are shown for three different redshifts  $z = 2, 3, 4$  as dashed, continuous and dotted curve, respectively. Note that the flux power spectra have not been scaled to reproduce the same effective optical depth.

proportion of absorption by dense shock-heated gas at  $z = 2$ .

- The HPM implementation of GADGET-2 and the code by GH give similar results (to within a few percent) for the same initial conditions, provided a slightly higher resolution of the PM grid is used for GADGET-2. This offset is a result of the PM force smoothing done by GADGET-2, which is adjustable. The results obtained above should thus hold in a similar form for the GH code.

The HPM method involves two main simplifications compared to full hydro-simulations, calculating the pressure in an approximate way and estimating the temperatures based on the density alone. The HPM approximation does a good job in modelling the gas and matter distribution on the scales relevant for the Lyman- $\alpha$  forest suggesting that the first approximation works well. The situation for an accurate prediction of the flux distribution is quite different and we have shown that the treatment of the thermal state in the HPM approximation is the main problem for accurate predictions of the flux distribution. The strong dependence of the transmitted flux on the thermal state of the gas together with the crude approximation of the thermal state in the HPM approximation leads to large and not always intuitive scale- and redshift-dependent differences in the flux distribution between HPM and the full hydrodynamical simulations.

For the flux power spectrum, these differences are less important than for the pdf of the flux distribution. Our results suggest that at  $z = 3$  and  $z = 4$  the gain in speed offered by HPM simulations may still make

them an attractive tool to obtain predictions of the flux power spectrum for a wide range of parameters. This will, however, require very careful calibration with full hydrodynamical simulations, and it appears doubtful that HPM simulations are suitable to model the dependence of the flux power spectrum on the thermal state of the gas accurately. The rather large memory requirement of HPM simulations with sufficient resolution to reach convergence also partially offsets the advantage of their higher speed. Our results further suggest that at lower redshift the larger proportion of absorption by dense shock-heated gas makes HPM simulations unsuitable for accurate predictions of the flux power spectrum.

Currently the observational uncertainties regarding the thermal state of the IGM are still rather large. The results of quantitative studies of the matter power spectrum with Lyman- $\alpha$  forest data are therefore generally marginalized over a wide range of simple temperature-density relations. The difficulties of simple HPM implementations with modeling the effect of the thermal state accurately may therefore be less important than suggested by our discussion so far. However, improved measurements of the thermal state of the gas utilizing the Doppler parameter distribution, the flux PDF and the small scale flux power spectrum are an important prerequisite for reducing the errors of measurements of the matter power spectrum from Lyman- $\alpha$  forest data.

Accurate modeling of the thermal state of the gas will be required to take full advantage of a reduced uncertainty regarding the thermal state of the IGM. For HPM simulations this will almost certainly require a significant improvement of the modelling of the ther-

mal state, e.g. by introducing some scatter in the temperature density relation. Full hydrodynamical simulations could thereby be used to quantify and calibrate this scatter and to investigate possible correlations of the scatter with physical quantities. Such modelling would obviously greatly benefit from more precise observational estimates of the parameters describing the temperature-density relation which may be possible with the use of the flux power at smaller scales and from an estimate of the scatter in the temperature density relation using higher order statistics such as the bispectrum (Mandelbaum et al. 2003, Viel et al. 2004, Fang & White 2004). It will then also be important (in HPM and full hydro simulations) to model other physical aspects affecting the thermal state of the gas as the presence of galactic winds and temperature/UV fluctuations due to the reionization of HeII.

## ACKNOWLEDGEMENTS.

The simulations were run on the COSMOS (SGI Altix 3700) supercomputer at the Department of Applied Mathematics and Theoretical Physics in Cambridge and on the Sun Linux cluster at the Institute of Astronomy in Cambridge. COSMOS is a UK-CCC facility which is supported by HEFCE and PPARC. MV thanks PPARC for financial support and Adam Lidz for useful discussions. MV, MGH and VS thank the Kavli Institute for Theoretical Physics in Santa Barbara, where part of this work was done, for hospitality during the workshop on “Galaxy-Intergalactic Medium Interactions”. This work is partly supported by the European Community Research and Training Network “The Physics of the Intergalactic Medium”. We thank Nick Gnedin for providing us with a copy of his HPM code.

## REFERENCES

- Abel T., Haehnelt M.G., 1999, ApJ, 520, L13  
 Bi H.G., 1993, ApJ, 405, 479  
 Bi H.G., Davidsen A.F., 1997, ApJ, 479, 523  
 Bolton J.S., Haehnelt M.G., Viel M., Springel V., 2005, MNRAS, 357, 117  
 Croft R. A. C., Weinberg D. H., Katz N., Hernquist L., 1998, ApJ, 495, 44  
 Croft R. A. C., Weinberg D. H., Pettini M., Hernquist L., Katz N., 1999, ApJ, 520, 1  
 Croft R. A. C., Weinberg D. H., Bolte M., Burles S., Hernquist L., Katz N., Kirkman D., Tytler D., 2002, ApJ, 581, 20  
 Desjacques V., Nusser A., 2004, astro-ph/0410618  
 Desjacques V., Nusser A., Haehnelt M.G., Stoher F., 2004, MNRAS, 350, 879  
 Eisenstein D. J., Hu W., 1999, ApJ, 511, 5  
 Fang T., White M., 2004, ApJ, L9  
 Gnedin N. Y., Hui L., 1996, ApJ, 472, L73  
 Gnedin N. Y., Hui L., 1998, MNRAS, 296, 44  
 Gnedin N. Y., Hamilton A. J. S., 2002, MNRAS, 334, 107  
 Hui L., Gnedin N., Zhang Y., 1997, ApJ, 486, 599  
 Hui L., Gnedin N., 1997, MNRAS, 292, 27  
 Hui L., Burles S., Seljak U., Rutledge R. E., Magnier E., Tytler D., 2001, ApJ, 552, 15  
 Kim, T.-S., Viel M., Haehnelt M.G., Carswell R.F., Cristiani S., 2004, MNRAS, 347, 355  
 Mandelbaum R., McDonald P., Seljak U., Cen R., 2003, MNRAS, 344, 776  
 McDonald P., Miralda-Escudé J., Rauch M., Sargent W.L., Barlow T.A., Cen R., Ostriker J.P., 2000, ApJ, 543, 1  
 McDonald P., 2003, ApJ, 585, 34  
 McDonald P. et al., 2004a, astro-ph/0407377  
 McDonald P. et al., 2004b, astro-ph/0407378  
 McGill C., 1990, MNRAS, 242, 544  
 Meiksin A., White M., 2001, MNRAS, 324, 141  
 Meiksin A., Bryan G., Machacek M., 2001, MNRAS, 327, 296  
 Rauch M., 1998, ARA&A, 36, 267  
 Ricotti M., Gnedin N., Shull M., 2000, ApJ, 534, 41  
 Schaye J., Theuns T., Rauch M., Efstathiou G., Sargent W. L. W., 2000, MNRAS, 318, 817  
 Springel V., Yoshida N., White S. D. M., 2001, NewA, 6, 79  
 Springel V., Hernquist L., 2002, MNRAS, 333, 649  
 Springel V., Hernquist L., 2003, MNRAS, 339, 289  
 Theuns T., et al., 1998, MNRAS, 301, 478  
 Viel M., Matarrese S., Mo H.J., Haehnelt M.G., Theuns T., 2002a, MNRAS, 329, 848  
 Viel M., Matarrese S., Mo H.J., Theuns T., Haehnelt M.G., 2002b, MNRAS, 336, 685  
 Viel M., Matarrese S., Theuns T., Munshi D., Wang Y., 2003, MNRAS, 340, L47  
 Viel M., Matarrese S., Heavens A., Haehnelt M., Kim T.-S., Springel V., Hernquist L., 2004, MNRAS, 347, L26  
 Viel M., Haehnelt M.G., Springel V., 2004, MNRAS, 354, 684  
 Viel M., Weller J., Haehnelt M.G., 2004, MNRAS, 355, L23  
 Viel M., Haehnelt M. G., Carswell R. F., Kim T.-S., 2004a, MNRAS, 349, L33  
 Weinberg D., 1999, in: Evolution of large scale structure : from recombination to Garching, eds. A. J. Banday, R. K. Sheth, L. N. da Costa., p.346  
 Zhan H., Davé R., Eisenstein D., Katz N., 2005, astro-ph/0504419